INSTITUTE OF PHYSICS PUBLISHING JOURNAL OF PHYSICS D: APPLIED PHYSICS

J. Phys. D: Appl. Phys. **34** (2001) 3368–3377 PII: S0022-3727(01)26864-8

Self-consistent modelling of helium discharges: investigation of the role of He_2^+ ions

Kinga Kutasi, Péter Hartmann and Zoltán Donkó

Research Institute for Solid State Physics and Optics, Hungarian Academy of Sciences, POB 49, H-1525 Budapest, Hungary

E-mail: kutasi@sunserv.kfki.hu

Received 13 July 2001
Published 20 November 2001
Online at stacks.iop.org/JPhysD/34/3368

Abstract

Helium glow discharges in the $p = 6$–60 mbar pressure range have been investigated experimentally and by means of a one-dimensional self-consistent hybrid model. Unlike most of the hybrid models developed previously for noble gas discharges, our model also includes He_2^+ molecular ions. The electrical parameters of the discharges, recorded in the experiments, as well as the electron temperature for the different discharge conditions (determined spectroscopically) have been used as input data for the hybrid model. Our studies show that He_2^+ ions are present in the discharge even at 6 mbar with a concentration comparable to that of He^+ ions. Conversion of atomic to molecular ions and the associative ionization process are identified as main sources of molecular ions. At low pressures the He_2^+ ions are principally lost at the electrodes, while at higher pressures the recombination processes become their dominant losses. As the rates of recombination processes are strongly pressure-dependent, the optical emission spectrum changes with increasing pressure and shows significant intensity of He_2 molecular bands. The contribution of He_2^+ ions to the ion current at the cathode as well as their contribution to maintenance of the discharge is found to be around 10%, even at the lowest pressure of 6 mbar, where He_2^+ formation in most of the discharge models is neglected.

1. Introduction

Helium discharges are extensively used in a wide range of applications, e.g. for spectral and illumination light sources, as well as for different types of lasers. In some of these sources He_2^+ molecular ions play an important role in the discharge processes. Even at relatively low pressures, in the 10–100 mbar range, helium molecular ions are assumed to influence the discharge conditions and/or participate in the pumping mechanism of the He–Cd^+ laser [1, 2] and the He–Zn^+ laser [3]. He_2^+ molecular ions have also been found to be responsible for the excitation in the He–Ar^+ laser [4, 5]. Similarly, they play an important role in the discharges formed in plasma addressed liquid crystal displays (operated in H_2+He mixtures at $p \sim 100$ mbar pressures) [6].

In helium discharges at higher pressures, UV and VUV lasers can be realized, e.g. the He–N_2^+ laser which is pumped by a very efficient reaction between helium molecular ions and nitrogen molecules [7, 8]. The UV and VUV radiation of helium discharge lamps originates from the excited He_2 and He_2^+ molecules [9]. As the ground state of He_2 molecule is unstable, the excited He_2 molecules result mainly from the recombination of He_2^+. High-pressure helium discharges are also used in analytical chemistry to detect traces of nonmetal analytes. Motivated by this particular application, helium discharges at atmospheric pressure have been extensively investigated by collisional radiative models [10, 11].

Hybrid models of low-pressure noble gas discharges usually consider only the presence of a single species of positive ions (the situation can be far more complicated in

molecular gases, e.g. H_2 [12, 13]). As an exception, a study of a low-pressure argon analytical glow discharge has to be mentioned [14]. To our best knowledge, however, the effects related to molecular ion formation in the cathode region of noble gas glow discharges have not yet been investigated by self-consistent modelling, except for the above paper. He_2^+ ions are expected, on the other hand, to be present in discharges at relatively low pressures, as indicated by the calculations for positive column discharges, where molecular helium ions were found to become the dominant ionic species at pressures exceeding ≈15 mbar [15]. In this paper we present our studies on helium glow discharges in the 6–60 mbar pressure range, comprising experimental investigations and self-consistent modelling of the discharge using a hybrid approach. The aim of our studies is to observe how the molecular helium ions become important in the discharge with increasing pressure and to identify the important source and loss processes of atomic and molecular ions as a function of pressure. The model includes several elementary processes that are believed to be important for the discharge conditions covered here, namely collisions of electrons and metastable atoms with ground state and metastable atoms, deexcitation, associative ionization, as well as ion conversion and recombination processes.

Section 2 of the paper describes the experimental arrangement. In section 3 the Monte Carlo, fluid and metastable models and their interfacing are outlined. The experimental and the modelling results are presented and discussed in section 4. The summary of the work is given in section 5.

2. Experimental setup

The discharge tube used in the experiment has three discharge cells, each having flat disk copper electrodes of 3.6 cm diameter and electrode gaps of 1, 0.3 and 0.1 cm, respectively. This arrangement makes it possible to realize 'similar' discharges in a wide pressure range. The whole construction is placed inside a Pyrex tube which is connected to a vacuum system having a base pressure of $\approx 10^{-6}$ mbar. Helium gas of 5.0 purity is used in the measurements. To avoid the excitation of N_2^+ molecular bands through the very efficient reaction between residual amounts of N_2 and He_2^+ molecules [16, 17], further purification of the filling gas by cataphoretic cleaning [18, 19] is employed. Helium is introduced into the discharge tube through an additional discharge having a 40 cm long positive column operated at 40 mA. The optical emission spectra recorded under these conditions show no emission on N_2^+ bands.

The discharges are operated in pulsed mode, excited by 0.8 ms long rectangular current pulses at 5 Hz repetition rate to reduce deposition due to cathode sputtering. The measurements are performed in the three discharge cells for different pressures (6 mbar $\leqslant p \leqslant$ 100 mbar) and current densities (0.9 mA cm^{-2} $\leqslant j \leqslant$ 100 mA cm^{-2}). The optical emission spectra of the discharges are recorded and their electrical characteristics are determined in the measurements. Additionally, the electron temperature (T_e) is also determined experimentally, by measuring the intensities of the spectral lines of the 2p ^{3}P–nd ^{3}D He I series. The optical emission spectra are measured by a 2 m monochromator equipped with an EMI 6256S photomultiplier tube (PMT). The signal of the PMT is fed to an HP54501A digitizing oscilloscope connected to a PC using an IEEE488 interface. The discharge voltage, current density and electron temperature serve as input data for the hybrid model.

3. Simulation model

The discharge is described by a one-dimensional hybrid model which combines a fluid model for atomic and molecular ions and slow electrons with Monte Carlo (MC) simulation of fast electrons, and with a diffusion-reaction model of the metastable species. The model makes it possible to calculate several discharge characteristics in a self-consistent way [20–25]. The elementary processes for electrons, ions and metastables taken into account in our model are listed in table 1, together with their cross sections or rate coefficients. For fast electrons we take into account elastic scattering (p1), excitation to metastable and several higher excited states (up to $n = 5$) (p2–p4) as well as ionization (p5). The excited atoms (including the $n = 3$ to $n = 5$ states) can participate in an associative ionization process (p6) in which molecular ions are created. The singlet and triplet atomic metastables convert into triplet atomic and molecular metastables, respectively, through reactions p7 and p8. The singlet atomic metastables also convert to ground state atoms due to the process p9. The atomic and molecular ions are created in the metastable–metastable ionization processes p10–p15 which result in the loss of metastables. The metastables are also lost in deexcitation processes p16–p18. The atomic ions convert into molecular ions due to the p19 conversion process. The atomic and molecular ions are lost through the collisional radiative recombination (p20–p21) and the three-body recombination (p22) processes.

To solve the hybrid model the 'apparent' secondary electron emission coefficient γ (the ratio of the electron current to the ion current at the cathode) has to be specified. The apparent γ coefficient accounts for all possible electron emission mechanisms [26]. Generally it is difficult to choose a proper value for γ which gives reasonable agreement with experimental data over a wide range of discharge conditions (pressure and current) [27]. Thus in our model we take γ as a variable (fitting) parameter. In the iterative solution of the model (at fixed discharge voltage) γ is adjusted to obtain a current density equal to the experimental value [28].

3.1. Fluid model of positive ions and slow electrons

The helium atomic and molecular ions and the slow electrons are treated together in a fluid model. The fundamental variables of the fluid model are the (slow) electron density n_e, the helium atomic ion density n_{i1}, the helium molecular ion density n_{i2} and the electrostatic potential V, which are functions of the axial coordinate x. The fluid model consists of the continuity equations of electrons and ions, and the Poisson equation:

$$\frac{\partial n_{e(i1)(i2)}}{\partial t} + \nabla(n_{e(i1)(i2)}\boldsymbol{v}_{e(i1)(i2)}) = S_{e(i1)(i2)} - L_{e(i1)(i2)}, \qquad (1)$$

$$\triangle V = -\frac{e}{\epsilon_0}(n_{i1} + n_{i2} - n_e), \qquad (2)$$

Table 1. Elementary processes considered in the model. The cross sections of processes p1–p5 are taken from [31]. The rate coefficients for p6–p22 are from [36]. In the processes p10–p15 the He^+ and He_2^+ ions are created with 0.3 and 0.7 probability, respectively.

Process identification	Reaction process	Cross section or rate coefficient
p1	$He + e^- \rightarrow He + e^-$	$\sigma(E)$
p2	$He + e^- \rightarrow He(T) + e^-$	$\sigma(E)$
p3	$He + e^- \rightarrow He(S) + e^-$	
p4	$He + e^- \rightarrow He^* + e^-$	
p5	$He + e^- \rightarrow He^+ + 2e^-$	$\sigma(E)$
p6	$He^* + He \rightarrow He_2^{+*} + e^-$	$k = 8 \times 10^{-17}\,m^3\,s^{-1}$
p7	$He(S) + e^- \rightarrow He(T) + e^- + 0.79\,eV$	$\kappa_s = 5 \times 10^{-15}\,m^3\,s^{-1}$
p8	$He(T) + 2He \rightarrow He(M) + He$	$\delta = 1.13 \times 10^{-1}\,mbar^{-2}\,s^{-1}$
p9	$He(S) + He \rightarrow 2He$	$\gamma = 8 \times 10^{-21}\,m^3\,s^{-1}$
p10	$He(S) + He(S) \rightarrow He^+ + He + e^- + 16.6\,eV$ $He_2^{+*} + e^- + 19\,eV$	$\beta_{ss} = 3.5 \times 10^{-15}\,m^3\,s^{-1}$
p11	$He(T) + He(T) \rightarrow He^+ + He + e^- + 15\,eV$ $He_2^{+*} + e^- + 17.4\,eV$	$\beta_{tt} = 1.5 \times 10^{-15}\,m^3\,s^{-1}$
p12	$He(S) + He(T) \rightarrow He^+ + He + e^- + 15.8\,eV$ $He_2^{+*} + e^- + 18.2\,eV$	$\beta_{st} = 3 \times 10^{-15}\,m^3\,s^{-1}$
p13	$He(S) + He_2(M) \rightarrow He^+ + 2He + e^- + 13.9\,eV$ $He_2^{+*} + He + e^- + 16.3\,eV$	$\beta_{sm} = 3 \times 10^{-15}\,m^3\,s^{-1}$
p14	$He(T) + He_2(M) \rightarrow He^+ + 2He + e^- + 13.1\,eV$ $He_2^{+*} + He + e^- + 15.5\,eV$	$\beta_{tm} = 2.5 \times 10^{-15}\,m^3\,s^{-1}$
p15	$He_2(M) + He_2(M) \rightarrow He^+ + 3He + e^- + 11.3\,eV$ $He_2^{+*} + 2He + e^- + 13.7\,eV$	$\beta_{mm} = 1.5 \times 10^{-15}\,m^3\,s^{-1}$
p16	$He(S) + e^- \rightarrow He + e^- + 20.6\,eV$	$\chi = 2.9 \times 10^{-15}\,m^3\,s^{-1}$
p17	$He(T) + e^- \rightarrow He + e^- + 19.8\,eV$	$\kappa_t = 4.2 \times 10^{-15}\,m^3\,s^{-1}$
p18	$He(M) + e^- \rightarrow He + e^- + 17.9\,eV$	$\kappa_m = 3.8 \times 10^{-15}\,m^3\,s^{-1}$
p19	$He^+ + 2He \rightarrow He_2^{+*} + He$	$\eta = 5.1 \times 10^{-1}\,mbar^{-2}\,s^{-1}$
p20	$He^+ + 2e^- \rightarrow He^* + e^-$	$k_{e1} = 6 \times 10^{-32}\,m^6\,s^{-1}$
p21	$He_2^{+*} + 2e^- \rightarrow He_2^* + e^-$	$k_{e2} = 4 \times 10^{-32}\,m^6\,s^{-1}$
p22	$He_2^{+*} + e^- + He \rightarrow He_2^* + He$	$k_{02} = 5 \times 10^{-39}\,m^6\,s^{-1}$

Note: He(S), He(T) and He(M) denote the singlet atomic, triplet atomic and molecular metastables, respectively.

where $\boldsymbol{v}_{e(i1)(i2)}$ are the mean velocities, $S_{e(i1)(i2)}$ are the source functions, $L_{e(i1)(i2)}$ are the loss functions of the slow electrons, atomic and molecular ions, respectively, e is the elementary charge and ϵ_0 is the permittivity of free space. The space charge created by the fast electrons—being several orders of magnitude smaller than that created by the slow electrons—is neglected in (2). The mean velocities are calculated from

$$\begin{aligned}\Phi_{e(i1)(i2)} &= n_{e(i1)(i2)}\boldsymbol{v}_{e(i1)(i2)} \\ &= Sn_{e(i1)(i2)}\mu_{e(i1)(i2)}\boldsymbol{E} - \nabla(n_{e(i1)(i2)}D_{e(i1)(i2)}),\end{aligned} \tag{3}$$

where $S = -1$ for electrons and $S = 1$ for ions, and $\mu_{e(i1)(i2)}$ and $D_{e(i1)(i2)}$ are the mobility and diffusion coefficients of electrons, atomic and molecular ions and $\Phi_{e(i1)(i2)}$ are the corresponding fluxes. The above simplified form of the momentum transfer equation (widely used in glow discharge modelling [20–22, 25]) involves only drift and diffusion terms and neglects the inertia term, because the motion of ions and slow electrons is assumed to be collisionally dominated. This assumption is valid for the slow electron group as they exist only in the low electric field region. Furthermore, Boltzmann equation analysis by Lawler [29] indicates that ions equilibrate relatively quickly in the cathode fall region. For our discharge conditions the ratio of the cathode fall length to the mean free path of ions is in the order of several tens to one hundred.

The mobility of electrons in helium is $\mu_e = (1/p)1.33 \times 10^6\,cm^2\,V^{-1}\,s^{-1}$ [30] (with p given in mbar) and the diffusion coefficient of electrons is chosen to be $D_e = \mu_e T_e$. The mobility of the helium atomic ions is taken from [31], and the data have been fitted to a functional form:

$$\mu_{i1} = \frac{11\,600}{p}\frac{1}{(1 + (0.045 \times E/p)^{1.26})^{0.41}}\,cm^2\,V^{-1}\,s^{-1}, \tag{4}$$

where units of E and p are $V\,cm^{-1}$ and mbar, respectively. The mobility of the molecular ions for $E/n \leqslant 43$ Td is taken from [32] and for higher reduced electric fields $E/n \geqslant 43$ Td μ_{i2} is approximated by [33]

$$\mu_{i2} = \frac{54 \times 10^{23}}{n}\left(\frac{40}{E/n}\right)^{0.3}\,cm^2\,V^{-1}\,s^{-1}, \tag{5}$$

where E/n is given in Td.

The diffusion coefficients of helium atomic and molecular ions are chosen as $D_{(i1)(i2)} = \mu_{(i1)(i2)}T_i$ with $T_i = 0.026\,eV$ (corresponding to a gas temperature of 300 K).

The source of slow electrons is calculated in the MC model. The sources of atomic and molecular ions resulting from processes p5–p6 and p10–p15 are calculated in the MC and in the metastable models, respectively. The source of molecular ions and the loss of atomic ions due to the ion conversion process (p19) are calculated from

$$S_{ci2}(x) = L_{ci1}(x) = \eta p^2 n_{i1}(x), \tag{6}$$

where η is the rate coefficient of the ion conversion process.

Examining the rates of different possible recombination processes, we find that the collisional radiative recombination (p20) dominates for He^+ ions, while the collisional radiative

(p21) and three-body recombination (p22) processes are significant for He_2^+. The loss of He_2^+ by dissociative recombination is found to be orders of magnitude smaller for our conditions [34, 35]. Taking into account these processes, the losses of charges can be determined from

$$L_{\mathrm{ri1}}(x) = k_{\mathrm{e1}} \left(\frac{T_\mathrm{e}}{T_\mathrm{g}}\right)^{-y_1} n_\mathrm{e}^2(x) n_{\mathrm{i1}}(x), \tag{7}$$

$$L_{\mathrm{ri2}}(x) = k_{02} n n_{\mathrm{i2}}(x) n_\mathrm{e}(x) \left(\frac{T_\mathrm{e}}{T_\mathrm{g}}\right)^{-x_2} + k_{\mathrm{e2}} n_{\mathrm{i2}}(x) n_\mathrm{e}^2(x) \left(\frac{T_\mathrm{e}}{T_g}\right)^{-y_2}, \tag{8}$$

$$L_{\mathrm{re}}(x) = L_{\mathrm{ri1}}(x) + L_{\mathrm{ri2}}(x), \tag{9}$$

where n is the background gas density, and T_e and T_g are the temperatures of the slow electron and the gas, respectively. The values of coefficients y_1, x_2, y_2 are taken from Deloche *et al* [36]: $y_1 = 4$, $x_2 = 1$ and $y_2 = 4$.

The fluid equations are solved using the Crank–Nicolson discretization scheme and an exponential representation of the fluxes [37]. The steady-state solution is obtained by an implicit time-integration technique [21, 22]; a detailed description of the numerical method can be found in previous works (e.g. [22]). The spatial grid had 101 points with uniform resolution. The boundary conditions at the wall are prescribed values for the potential and zero density of particles. The cathode potential is taken to be zero while the anode potential is set equal to the discharge voltage.

3.2. Monte Carlo model for the fast electrons

The motion of the fast electrons is traced using MC simulation. In this algorithm random numbers are used to determine the positions and the types of the collisions. The random numbers (R_{01}) have a uniform distribution in the [0,1) interval.

The initial energy of the electrons leaving the cathode is chosen randomly between 0 and 10 eV, and their initial velocity is set perpendicular to the cathode surface. The primary electrons emitted from the cathode and their secondaries produced in ionizing collisions are traced until they are absorbed by the anode or, due to their energy losses in inelastic collisions, they are no longer capable of producing any additional ions. The trajectory of electrons between successive collisions is followed by direct integration of their equation of motion. The free path of electrons is assigned randomly and the positions of the collisions are calculated from

$$\int_{s_0}^{s_1} n\sigma[\varepsilon(s)]\,\mathrm{d}s = -\ln(1 - R_{01}), \tag{10}$$

where s_0 is the position of the last collision, s_1 is the position of the next collision measured on the curvilinear abscissa s, n is the background gas density, σ is the sum of cross sections of all possible elementary processes and ε is the kinetic energy of the electron (see e.g. [41]).

The type of the collision which occurs after the free flight is chosen randomly, taking into account the values of cross sections of different processes at the energy of the colliding electron. In our calculation we take into account the elastic scattering of electrons from helium atoms, electron impact excitation and ionization of helium atoms. The cross sections of these elementary processes are taken from [31].

For the elastic scattering process the elastic momentum transfer cross section is used and isotropic scattering is assumed. The energy loss of the electrons is neglected.

Electron impact excitation to the two metastable levels (2^1S, 2^3S) and to the levels up to $n = 5$ is considered. The scattering angle and the azimuthal angle are taken to be random over the $[0, \pi]$ and the $[0, 2\pi]$ intervals, respectively.

In the ionization process the energy of the ejected and the scattered electrons is partitioned in accordance with the procedure described in [38–40]. The velocity vectors of the incoming, scattered and ejected electrons lie in the same plane and the scattering angles (measured with respect to the direction of velocity of the incoming electron) are found from the formula given in [41]. The azimuthal angle of the scattered electron is chosen randomly between 0 and 2π.

The source functions of atomic ions $S_{\mathrm{mci1}}(x)$ and of metastables $S_{\mathrm{s(t)}}(x)$ are accumulated from the individual ionization and excitation processes, respectively. The electrons are transferred to the slow electron group (through the $S_\mathrm{e}(x)$ source function) when their (kinetic + potential) energy falls below the ionization potential of the helium atoms. Here the potential energy is defined as the difference between the maximum value of the potential in the discharge and the potential at the actual position of the electron.

In the MC model we also take into account the associative ionization process (p6). In this process the molecular helium ions are formed in collisions between excited atoms (excited to levels $n \geqslant 3$) and ground state atoms [42,43]. The source of molecular ions S_{mci2} created in this process is calculated from

$$S_{\mathrm{mci2}}(x) = k n^*(x) n, \tag{11}$$

$$n^*(x) = \frac{S^*(x)}{1/\tau + kn}, \tag{12}$$

where $n^*(x)$, $S^*(x)$ and τ are the density, source and lifetime of excited atoms [44], respectively, and n is the background gas density. The rate coefficient k is given in table 1. The fast electrons created in this process, $S_{\mathrm{fe}}(x) = S_{\mathrm{mci2}}(x)$, are followed in the MC model.

3.3. Metastable model

Metastable atoms and molecules play an important role in the creation of molecular and atomic ions. The transport and kinetics of metastables in the discharge are modelled using three balance equations which are coupled differential equations, taking into account the sources and losses due to processes p7–p18 listed in table 1 and the sources of metastables obtained in the MC simulation:

$$\frac{\partial n_\mathrm{s}}{\partial t} = D_\mathrm{s}\nabla^2 n_\mathrm{s} + S_\mathrm{s} - \gamma n_\mathrm{s} n - \kappa_\mathrm{s} n_\mathrm{e} n_\mathrm{s} - \beta_{\mathrm{ss}} n_\mathrm{s}^2 - \beta_{\mathrm{st}} n_\mathrm{s} n_\mathrm{t} - \beta_{\mathrm{sm}} n_\mathrm{s} n_\mathrm{m} - \chi_\mathrm{s} n_\mathrm{e} n_\mathrm{s} = 0, \tag{13}$$

$$\frac{\partial n_\mathrm{t}}{\partial t} = D_\mathrm{t}\nabla^2 n_\mathrm{t} + S_\mathrm{t} + \kappa_\mathrm{s} n_\mathrm{e} n_\mathrm{s} - \beta_{\mathrm{tt}} n_\mathrm{t}^2 - \beta_{\mathrm{st}} n_\mathrm{t} n_\mathrm{s} - \delta p^2 n_\mathrm{t} - \beta_{\mathrm{tm}} n_\mathrm{t} n_\mathrm{m} - \chi_\mathrm{t} n_\mathrm{e} n_\mathrm{t} = 0, \tag{14}$$

$$\frac{\partial n_\mathrm{m}}{\partial t} = D_\mathrm{m}\nabla^2 n_\mathrm{m} - \beta_{\mathrm{mm}} n_\mathrm{m}^2 - \beta_{\mathrm{tm}} n_\mathrm{m} n_\mathrm{t} + \delta p^2 n_\mathrm{t} - \beta_{\mathrm{sm}} n_\mathrm{m} n_\mathrm{s} - \chi_\mathrm{m} n_\mathrm{e} n_\mathrm{m} = 0, \tag{15}$$

where $n_{s(t)(m)}$ and $D_{s(t)(m)}$ are the density and diffusion coefficients of singlet and triplet atomic and molecular metastables, respectively, and β, δ, γ, κ, χ are the rate coefficients of the processes (see table 1). The diffusion coefficients are taken from [36]: $D_s p = 598.5\,\mathrm{cm^2\,mbar\,s^{-1}}$, $D_t p = 558.6\,\mathrm{cm^2\,mbar\,s^{-1}}$ and $D_m p = 405.65\,\mathrm{cm^2\,mbar\,s^{-1}}$. The time-independent (steady state) equations are solved directly (inverting tridiagonal matrices after discretization of the equations), the coupling between them is taken into account using iterations, until the error term can be neglected. The equations are solved numerically on the same grid as used in the solution of fluid equations. The boundary conditions at the wall are prescribed zero densities of metastables. Solving these equations the densities of atomic and molecular metastables are found, and the sources of the molecular and atomic ions created in the metastable–metastable collisions (p10–p15) can be calculated according to $S_{mi1} = 0.3S_m$ and $S_{mi2} = 0.7S_m$, where

$$S_m(x) = \beta_{ss} n_s^2(x) + \beta_{tt} n_t^2(x) + \beta_{st} n_t(x) n_s(x) + \beta_{mm} n_m^2(x) + \beta_{tm} n_m(x) n_t(x) + \beta_{sm} n_m(x) n_s(x). \quad (16)$$

The factors 0.3 and 0.7 express the probability of the creation of atomic and molecular ions in metastable–metastable collisions [36].

In the metastable deexcitation processes p16–p18, slow electrons are lost: the loss of these electrons can be calculated from

$$L_{me}(x) = \chi_m n_e(x) n_m(x) + \chi_t n_e(x) n_s(x) + \chi_s n_e(x) n_t(x). \quad (17)$$

The fast electrons created in processes p10–p18 with energies ranging between 15 and 19 eV are treated in the MC model. The source of these fast electrons is calculated from

$$S_{fe}(x) = \beta_{ss} n_s^2(x) + \beta_{st} n_s(x) n_t(x) + \beta_{tt} n_t^2(x) + \beta_{sm} n_s(x) n_m(x) + \beta_{mm} n_m^2(x) + \beta_{tm} n_m(x) n_t(x). \quad (18)$$

3.4. Combination of the models

In our model the fluid, MC and metastable models are solved in an iterative way until the stationary state of the discharge is reached. In the first step of the iterations the fluid model is solved to obtain an 'initial' electric field distribution, and the avalanches initiated by a given number of primary electrons (N_0) are traced afterwards by the MC simulation. After completing the MC simulation cycle, the ion, slow electron and metastable source functions $S_e(x)$, $S_{mci1}(x)$, $S_{(s,t)}(x)$ are normalized by the actual value of the current I (calculated in the previous fluid cycle):

$$S(x) = \frac{I}{e(1+1/\gamma)\triangle V_x} \frac{N_x}{N_0}, \quad (19)$$

where N_x is the number of ions (slow electrons, metastables) created in a cell with volume $\triangle V_x$ around x. Using the metastable source functions calculated in the MC cycle, the metastable model is solved to obtain the sources of the atomic and molecular ions. In the next step the fluid model is solved using the ion and electron sources and losses obtained in the MC and metastable cycle.

The typical integration time step in the fluid model is in the order of 10 ns; the MC and metastable parts are usually run after 100 steps in the fluid model. Typically 1000 primary electrons and their secondaries are traced in the MC procedure. Having obtained the converged solution, the MC simulation is run once more for 2×10^5 primary electrons to obtain sufficiently smooth source functions. As has already been mentioned in the iterative solution of the hybrid model, the γ coefficient is adjusted in a way that the calculated current converges to its experimental value.

4. Results and discussion

4.1. Experimental results

Figure 1 shows the spectra of the discharges recorded in the 4620–4720 Å spectral range for three sets of discharge conditions: (a) $p = 6$ mbar, $I = 10$ mA, $L = 1$ cm, (b) $p = 20$ mbar, $I = 111$ mA, $L = 0.3$ cm, and (c) $p = 60$ mbar, $I = 1$ A, $L = 0.1$ cm. These conditions correspond to the same $pL = 6$ mbar cm and reduced current density $j/p^2 = 0.027\,\mathrm{mA\,cm^{-2}\,mbar^{-2}}$. At the lowest pressure ($p = 6$ mbar) only He I and He II lines appear in the spectrum. At $p = 20$ mbar, besides the He atomic and ion lines the (0, 0) band of the He_2 $3p\pi\ e^3\Pi_g$–$2s\sigma\ a^3\Sigma_u^+$ transition [45, 46] appears with a low intensity in the above wavelength range. At higher pressure ($p = 60$ mbar) the intensity of this band becomes comparable to that of the He I and He II lines. As the ground state of the He_2 molecule is unstable, the excited He_2 molecules cannot be created by electron impact excitation

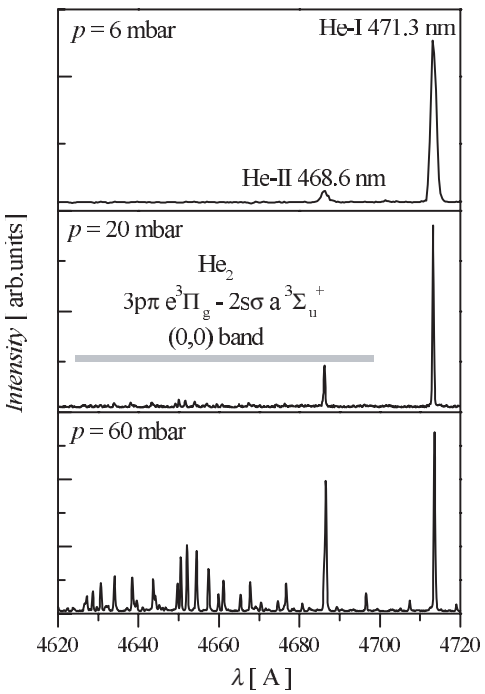

Figure 1. Optical emission spectra of the discharges between 4620 and 4720 Å at different pressures. The difference in the width of spectral lines is due to the different monochromator slit widths used at different pressures.

(except from the expectedly less populated He_2 $a^3\Sigma$ metastable state); they result mainly from the recombination of the He_2^+ molecules [47, 48]. The high intensity of the He_2 bands at high pressures ($p > 20$ mbar) indicates that in this pressure range a high density of He_2^+ molecules is present and efficient recombination channels exist in the discharge plasma.

The electron temperature is determined by measuring the intensities of the spectral lines of the 2p ^{3}P–nd ^{3}D He I series ($n \geqslant 6$). The upper levels of these transitions are near the ionization limit and hence interact strongly with the low-energy electrons. The measurement of T_e using this spectroscopic technique requires a local thermal equilibrium to exist among these states. According to the criteria formulated by Griem [49], this requires an electron density in excess of $\approx 4 \times 10^{11}$ cm^{-3}; this condition is satisfied at our discharge conditions.

The intensity of a transition is given by

$$I(n \to 2) = A_{n2} N_n hc/\lambda_{n2}, \tag{20}$$

where A_{n2} is the nd ^{3}D $\to$ 2p ^{3}P transition probability [50], N_n is the population of the upper state and λ_{n2} is the wavelength of the radiation. From this equation the population of the levels can be determined, and assuming that the levels are in local thermodynamic equilibrium their populations are related to each other by the Boltzmann factor:

$$\frac{N_m}{N_n} = \frac{g_m}{g_n} \exp - \frac{E_m - E_n}{kT_e}. \tag{21}$$

Consequently

$$\ln \frac{1}{N_m} - \ln \frac{1}{N_n} = \text{const} + \frac{E_m - E_n}{kT_e}, \tag{22}$$

where $g_{n(m)}$ and $E_{n(m)}$ are the statistical weight and the energy of level $n(m)$, respectively. According to equation (22) the inverse of the slope of the line connecting the data points $\ln(1/N_n)$ versus E_n yields the electron temperature. In the following T_e is given in units of electron volts.

Figure 2(a) shows a typical spectrum measured in the 3575–3830 Å spectral range. The spectrum is shown for the $L = 0.3$ cm cell at $p = 20$ mbar pressure and the transitions used in the calculation of T_e are marked. Figure 2(b) shows $\ln(1/N_n)$ plotted versus E_n for the 1, 0.3 and 0.1 cm discharge cells for $pL = 6$ mbar cm and $j/p^2 = 0.027$ mA cm^{-2} mbar^{-2} discharge conditions. Although the pL = const and j/p^2 = const similarity relations hold for these discharges [51], the optical emission spectra have already suggested that they are not truly similar. The plots show that $\ln(1/N_n)$ depends linearly on E_n, which means that the levels are in local thermodynamic equilibrium and thus the electron temperature of slow electrons can be determined. The electron temperatures obtained from these data are in the range of 0.1–0.12 eV. These values agree very well with previously reported experimental data for T_e; see e.g. [52]. The error of our T_e data is less than 20%. The study of the current dependence of the electron temperature shows that T_e decreases slightly with increasing current. In the case of the 0.1 cm cell at 60 mbar pressure and 0.4 A current T_e has been found to be 0.114 eV, at $I = 0.7$ A $T_e = 0.108$ eV and at 1 A current the electron temperature is 0.104 eV (these changes are, however, within the uncertainty of our measurements).

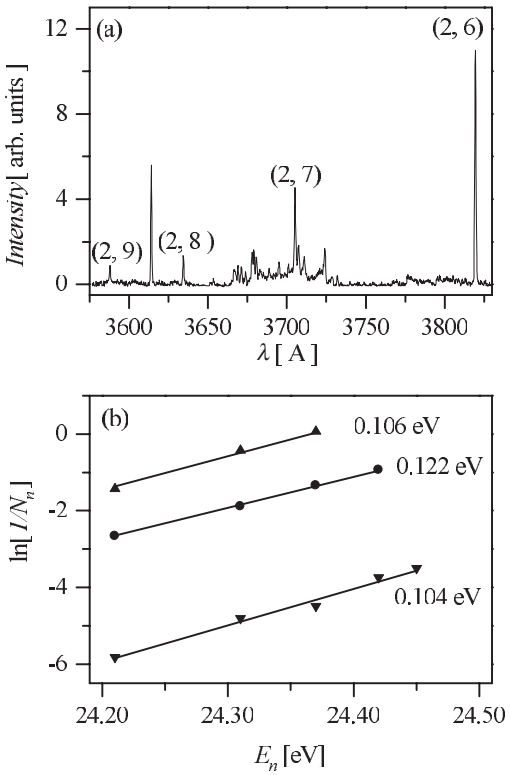

Figure 2. (a) Optical emission spectrum covering the 2p ^{3}P–nd ^{3}D He I series at $p = 20$ mbar. (b) $\ln(1/N_n)$ as a function of E_n at different pressures: $p = 6$ mbar (▲), $p = 20$ mbar (●) and $p = 60$ mbar (▼).

4.2. Results of the simulations

In this section the simulation results are presented. First we illustrate the general properties of the discharges. Following this, the effect of the pressure is illustrated. Figure 3 shows the discharge characteristics for the $L = 0.3$ cm discharge cell at $p = 20$ mbar pressure, $I = 111$ mA current and $V = 350$ V voltage. In figure 3(a) the electric field distribution is presented. The formation of the sheath near the cathode is clearly visible. At the cathode a high electric field is present ($\approx$8000 V cm^{-1}), and the electric field decreases nearly linearly in the sheath [53]. In the negative glow region the field reverses and at the anode a small negative field is present [54, 55]. The small negative field drives some of the ions created in the negative glow to the anode, while the electrons diffuse to the anode against this weak field. This is illustrated in figure 3(b), where the particle fluxes are presented. In figure 3(b) the metastable fluxes are also displayed. The ions and metastables reaching the cathode contribute to the electron emission from the cathode, assuring the self-sustainment of the discharge. Figure 3(b) shows that the fluxes of the metastables are two orders of magnitude smaller than the fluxes of ions. As the secondary yield of metastables is nearly the same as that of the ions [56], the electrons are released from the cathode mainly due to the ions. At the cathode the ratio of the fluxes of He^+ to He_2^+ is about 5.3. As the secondary yield of He_2^+ ions is expected to be about 60% of He^+ [56, 57], $\approx$90% of electrons are released by the atomic ions.

Figure 3(c) shows the distribution of the ion (atomic + molecular) and slow electron densities as well as the density

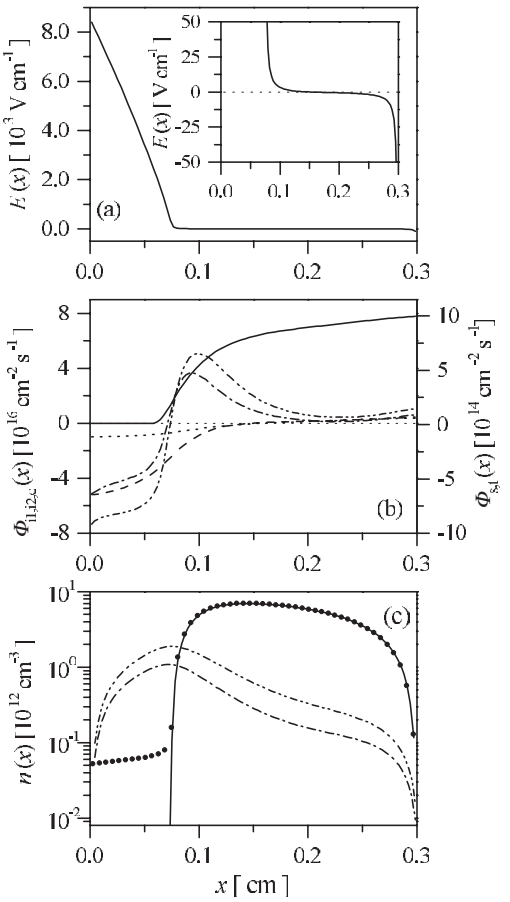

Figure 3. Discharge characteristics for $p = 20$ mbar, $V = 350$ V and $I = 111$ mA: (*a*) distribution of the electric field along the x axis; (*b*) slow electron (——), atomic (– – –) and molecular (· · · · · ·) ion, singlet (— · —) and triplet (— · · —) metastable fluxes; (*c*) density of the slow electrons (——), ions (atomic + molecular) (●), singlet (— · —) and triplet (— · · —) metastables as a function of axial position.

of the singlet and triplet atomic metastables. In the vicinity of the cathode, the positive space charge is dominant and the ion density is $\approx 5 \times 10^{10}$ cm^{-3}. Further away from the cathode (in the negative glow), the densities of ions and slow electrons become equal (with a peak value of $\approx 7 \times 10^{12}$ cm^{-3}) and a quasi-neutral plasma is formed. Near the cathode fall–negative glow boundary, the density of slow electrons rapidly decreases towards the cathode fall region. This result is in agreement with the observation of other authors [20, 22, 25] on similar discharges. The physical reason for the fast decay of slow electron density is that the slow electrons (born in the negative glow region) have small characteristic energy (typically <1 eV, and ≈0.1 eV found in our experiment) and thus they cannot penetrate into the cathode fall region due to the electric field present there. It is noted that figure 3(*c*) does not include the density of fast electrons, which are traced by MC simulation. It has also been shown however [25] that for typical glow discharge conditions the density of fast electrons is about three orders of magnitude smaller compared to the positive ion density. Consequently the space charge present in the cathode fall region can be considered as created only by positive ions. The density of metastables is maximum at the cathode sheath–negative glow boundary. Figure 3(*c*) shows that in the discharge the triplet metastables dominate, and the ratio of the maximal triplet to maximal singlet metastable density is ≈2, due to the high rate of the singlet to triplet conversion process (p7). From the metastable model it has also been found that the density of molecular metastables is seven orders of magnitude smaller than that of atomic metastables. Thus the contribution of the molecular metastables to the production of atomic and molecular ions can be neglected. Consequently the processes involving molecular metastables p13–p15 and p18 are unimportant.

In the following the simulation results are presented for three cases: (a) $p = 6$ mbar, $I = 10$ mA, $L = 1$ cm, (b) $p = 20$ mbar, $I = 111$ mA, $L = 0.3$ cm, and (c) $p = 60$ mbar, $I = 1$ A, $L = 0.1$ cm. These conditions correspond to the same $pL = 6$ mbar cm and reduced current density $j/p^2 = 0.027$ mA cm^{-2} mbar^{-2}.

Figure 4 shows the source and loss functions for the atomic ions for the three different sets of conditions. The source of ions has its maximum at the cathode sheath–negative glow boundary (located at $\approx \frac{1}{5}$ of the gap). At each set of conditions the main source of atomic ions is the electron impact ionization both in the cathode sheath and in the negative glow region. The relative contribution of this process and the metastable–metastable ionization to the production of atomic

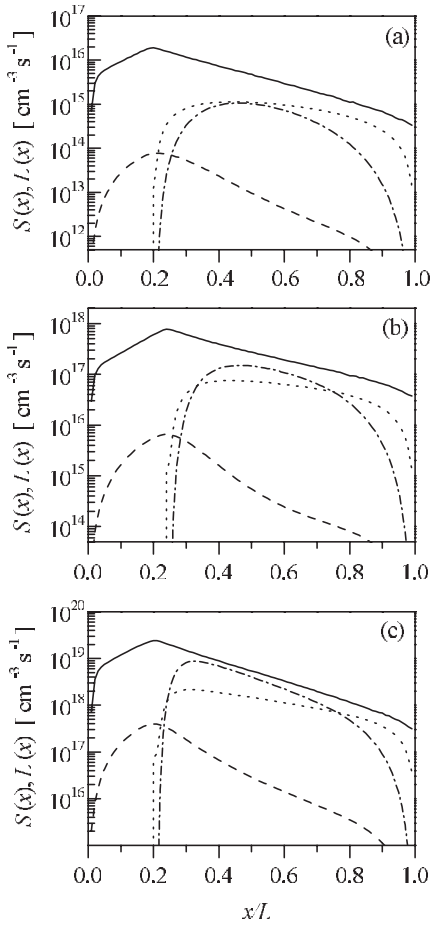

Figure 4. Sources of atomic ions due to electron impact ionization (——), metastable–metastable ionization (– – –), and losses due to ion conversion (· · · · · ·) and collisional radiative recombination (— · —). (*a*) $p = 6$ mbar and $L = 1$ cm, (*b*) $p = 20$ mbar and $L = 0.3$ cm, (*c*) $p = 60$ mbar and $L = 0.1$ cm.

Table 2. Relative contributions of different processes to the source and loss of He^+ ions at different pressures for constant reduced current density $j/p^2 = 0.027\,\mathrm{mA\,cm^{-2}\,mbar^{-2}}$.

	Production %		Loss %		
Pressure (mbar)	Electron impact ionization	Metastable–metastable ionization	Loss at electrodes	Ion conversion	Collisional radiative recombination
6	99.7	0.3	85	9	6
20	99.5	0.5	69	13	18
60	98.9	1.1	58	12	30

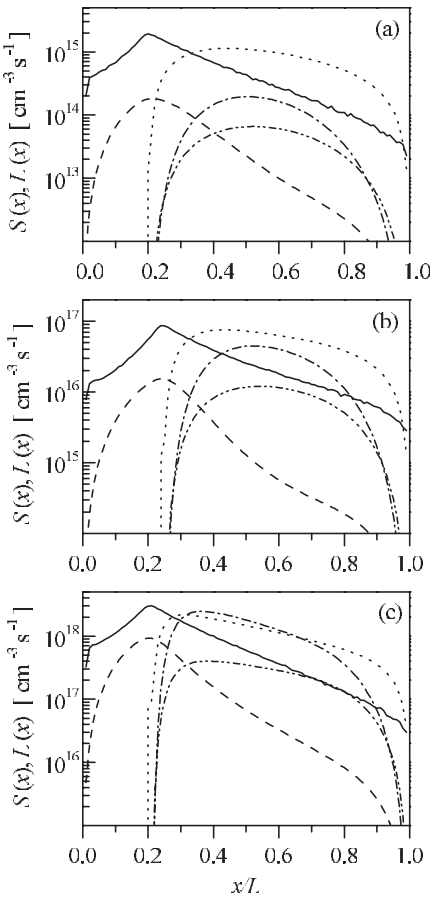

Figure 5. Sources of molecular ions due to associative ionization (——), metastable–metastable ionization (– – –), ion conversion (· · · · · ·), and losses due to collisional radiative recombination (— · —) and three-body recombination (— · · —). (*a*) $p = 6$ mbar and $L = 1$ cm, (*b*) $p = 20$ mbar and $L = 0.3$ cm, (*c*) $p = 60$ mbar and $L = 0.1$ cm.

ions varies slightly with pressure; see table 2. In table 2 the relative contributions of loss processes are also listed. At low pressures the ions are mainly lost at the electrodes (at $p = 6$ mbar 85%). With increasing pressure the importance of the collisional radiative recombination and ion conversion processes increases; at $p = 60$ mbar 30% of the ions are lost due to recombination and 12% by conversion to molecular ions.

Figure 5 shows the source and loss functions for the molecular ions. Similarly to the case of He^+ ions, the source of He_2^+ is maximum at the cathode sheath–negative glow boundary. In the cathode sheath the molecular ions originate mainly from the associative ionization process, while in the negative glow region the main source of molecular ions is ion conversion and associative ionization. The relative contributions of the production processes to the source of He_2^+ vary slightly with pressure; see table 3. At low pressure the molecular ions are mainly lost at the electrodes (at $p = 6$ mbar 92%). With increasing pressure the importance of the recombination processes increases (see table 3) and at 60 mbar they become the dominant loss processes for He_2^+ ions. At 60 mbar 44% of molecular ions are lost due to the collisional radiative recombination while 9% are lost in the three-body recombination process.

Figure 6 shows the calculated charge densities. It can be observed that the electron, atomic and molecular ion densities have their maxima at different positions (the electron density does not include the fast electrons, as discussed in figure 3(*c*)). The results show that the ratio of the maximal atomic to maximal molecular ion density decreases with increasing pressure. At $p = 6$ mbar this ratio is about 3.42, and at $p = 60$ mbar it becomes 2.2. At $p = 60$ mbar, at the anode side of the negative glow the molecular ion density exceeds the atomic ion density (see figure 6(*c*)). It has to be noticed that even at low pressure ($p = 6$ mbar) there is a significant He_2^+ ion density in the discharge. The lack of radiation on molecular bands at such low pressures can be explained by the slow recombination rate of He_2^+ ions. As we have seen above, with increasing pressure the recombination rate increases significantly resulting in the appearance of molecular bands in the emission spectrum (see figure 1).

The field reversal in the negative glow region exists for all the conditions studied; consequently a fraction of ions, which are not recombined in the negative glow region, move toward the anode. At $p = 6$ mbar pressure, ≈10% of atomic ions and ≈30% of molecular ions move to the anode. With increasing pressure the flux of ions at the anode decreases, and at $p = 60$ mbar only ≈1% of atomic and ≈9% of molecular ions flow to the anode. The contribution of these ions to the current at the anode is small; at $p = 6$ mbar 11.5% of the current is carried by the ions while at $p = 60$ mbar only 2%. At the cathode the current is carried mainly by the ions (≈86% at $p = 6$ mbar, varying slightly with pressure). At $p = 6$ mbar, ≈74% of the current is carried by the atomic ions and ≈12% by the molecular ions. With increasing pressure the contribution of molecular ions to the current increases slightly (≈13% at $p = 60$ mbar), while the contribution of atomic ions slightly decreases (≈69% at $p = 60$ mbar). Thus we can conclude that molecular ions play an important role in the carrying of current even at low pressures.

The apparent secondary electron emission coefficient γ (ratio of electron to ion current density at the cathode) at 6 mbar is found to be 0.16. At 20 mbar γ is 0.113 and at 60 mbar γ increases to 0.222.

Table 3. Relative contributions of different processes to the source and loss of He_2^+ ions at different pressures for constant reduced current density $j/p^2 = 0.027\,\mathrm{mA\,cm^{-2}\,mbar^{-2}}$.

	Production %			Loss %		
Pressure (mbar)	Associative ionization	Metastable–metastable ionization	Ion conversion	Loss at electrodes	Collisional radiative recombination	Three-body recombination
6	47	4	49	92	6	2
20	40	5	55	69	24	7
60	44	10	46	47	44	9

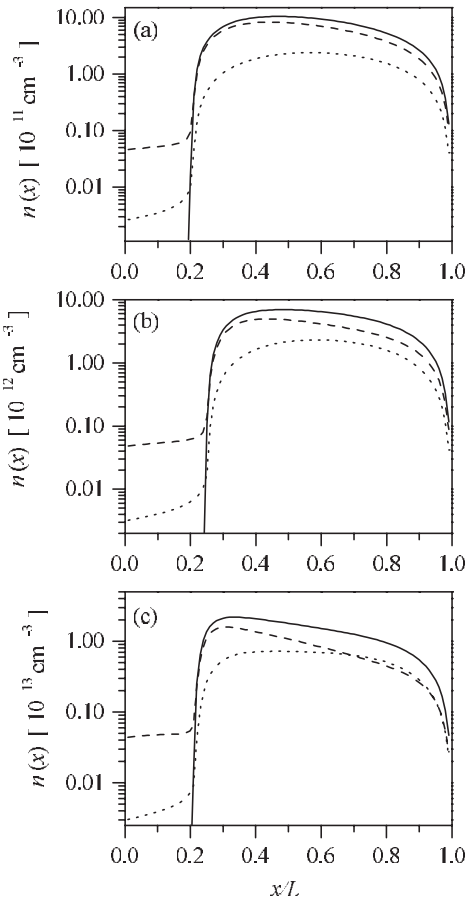

Figure 6. Density distribution of the slow electrons (——), atomic (– – –) and molecular (· · · · · ·) ions. (*a*) $p = 6$ mbar and $L = 1$ cm, (*b*) $p = 20$ mbar and $L = 0.3$ cm, (*c*) $p = 60$ mbar and $L = 0.1$ cm.

5. Summary

Helium glow discharges have been studied experimentally and by means of a one-dimensional self-consistent hybrid model. The high-energy electrons have been traced by MC simulation to provide a fully kinetic description of their motion. The transport and kinetics of metastables which play an important role in the formation of molecular and atomic ions have been modelled with a diffusion-reaction model, while a fluid model has been used for the slow electrons, atomic and molecular ions. The measurements have been carried out in the 6–60 mbar pressure range using three discharge cells of 0.1, 0.3 and 1 cm length, respectively. The calculations were made for three sets of discharge conditions: (a) $p = 6$ mbar, $I = 10$ mA, $L = 1$ cm, (b) $p = 20$ mbar, $I = 111$ mA, $L = 0.3$ cm, and (c) $p = 60$ mbar, $I = 1$ A, $L = 0.1$ cm, corresponding to the same $pL = 6$ mbar cm and reduced current density $j/p^2 = 0.027\,\mathrm{mA\,cm^{-2}\,mbar^{-2}}$.

The voltage–current characteristics of the discharge, the electron temperature as well as the optical emission spectra have been determined in the experiments. The measured electrical characteristics and the electron temperature are used as input data of our hybrid model. It has been found that in the 6–60 mbar pressure range and at 0.01–1 A current the electron temperature is in the range of 0.1–0.12 eV and at constant pressure T_e decreases slightly with increasing current. At low pressure only the He I and He II lines appear in the optical emission spectrum, while at high pressures the bands of the He_2 molecule appear beside the atomic and ion lines, indicating the presence of significant He_2^+ ion density in the discharge.

The simulation results have shown that in the negative glow region the electric field changes sign. This negative field drives some of the ions (atomic and molecular) to the anode, while the electrons have to diffuse to the anode against this weak field.

In the simulations the main sources and losses of the atomic and molecular ions have been identified. The main source of atomic ions is the electron impact ionization process. At low pressure the ions are mainly lost at the electrodes (e.g. 85% at $p = 6$ mbar). At higher pressures the ion conversion process and the collisional radiative recombination also become important (e.g. at $p = 60$ mbar 12% and 30%, respectively); however the main part of ions are still lost at the electrodes (58% at $p = 60$ mbar). The molecular ions are created mainly by associative ionization and ion conversion (at $p = 6$ mbar ≈47% and ≈48%), and the contributions of these processes vary slightly with pressure. At low pressures the molecular ions are mainly lost at the electrodes. With increasing pressure the importance of the recombination processes increases, becoming the dominant loss processes at $p = 60$ mbar. At $p = 60$ mbar 44% of He_2^+ ions are lost due to the collisional radiative recombination process and 9% due to the three-body recombination process.

The results show that the densities of He^+ and He_2^+ ions have their maxima at different positions. The ratio of the maximal atomic to the maximal molecular ion density decreased with increasing pressure; at $p = 6$ mbar this ratio is 3.42 and at $p = 60$ mbar it becomes 2.2.

The contribution of atomic and molecular ions to the ion current at the cathode has been determined from the charge fluxes. Molecular ions play an important role in the carrying of current, and their contribution increases slightly with increasing pressure. Molecular ions also play an important role in the self-sustainment of the discharge; ≈10% of the secondary electrons are released from the cathode by the molecular ions.

Acknowledgments

This work was supported by the Hungarian Science Foundation (Grants OTKA-T-25989 and T-34156) and the NATO Science for Peace programme (SfP-971989). We thank A V Phelps, A Bogaerts, M Jánossy, L Csillag and G Bánó for discussions. The construction of the discharge tube by T J Forgács, J Tóth, E Sárközi and Gy Császár is gratefully acknowledged.

References

[1] Telle H H, Hopkin I D, Ramalingam P, Fun H K and Grey Morgan C 1988 *J. Phys. D: Appl. Phys.* **21** S167
[2] Teuner D 2000 *PhD Thesis* Bochum
[3] Derzhiev V, Karelin A, Sereda O, Stefanova M and Yakovlenko S 1990 *Appl. Phys.* B **51** 465
[4] Mezei P and Jánossy M 1991 *Appl. Phys.* B **52** 295
[5] Csillag L and Jánossy M 1992 *Appl. Phys.* B **55** 401
[6] Hagelaar G J M, Kroesen G M W, van Slooten U and Schreuders H 2000 *J. Appl. Phys.* **88** 2252
[7] Collins C B, Cunningham A J and Stockton M 1974 *Appl. Phys. Lett.* **25** 344
[8] Rothe D E and Tan K O 1977 *Appl. Phys. Lett.* **30** 152
[9] Hill P C and Herman P R 1993 *Phys. Rev.* A **47** 4837
[10] Petrov G M, Matte J P, Peres I, Margot J, Sadi T, Hubert J, Tran K C, Alves L L, Loureiro J, Ferreira C M, Guerra V and Gousset G 2000 *Plasma Chem. Plasma Proc.* **20** 183
[11] Peres I, Alves L L, Margot J, Sadi T, Ferreira C M, Tran K C and Hubert J 1999 *Plasma Chem. Plasma Proc.* **19** 467
[12] Hantzsche E 1964 *Beitr. Plasmaphysik* **4** 165
[13] Hantzsche E 1969 *Beitr. Plasmaphysik* **9** 439
[14] Bogaerts A and Gijbels R 1999 *J. Appl. Phys.* **86** 4124
[15] Ichikawa Y and Teii S 1980 *J. Phys. D: Appl. Phys.* **13** 2031
[16] Collins C B, Cunningham A J, Curry S M, Johnson B W and Stockton M 1974 *Appl. Phys. Lett.* **24** 477
[17] Leventhal J J, Earl J D and Harris H H 1975 *Phys. Rev. Lett.* **35** 719
[18] Sosnowski T P 1969 *J. Appl. Phys.* **40** 5138
[19] Tombers R B, Gaur J P and Chanin L M 1971 *J. Appl. Phys.* **42** 4855
[20] Surendra M, Graves D B and Jellum G M 1990 *Phys. Rev.* A **41** 1112
[21] Boeuf J P and Pitchford L C 1991 *IEEE Trans. Plasma Sci.* **19** 286
[22] Fiala A, Pitchford L C and Boeuf J P 1994 *Phys. Rev.* E **49** 5607
[23] Donkó Z 1998 *Phys. Rev.* E **57** 7126
[24] Pedoussat C 1999 *PhD Thesis* Université Paul Sabatier
[25] Bogaerts A, Gijbels R and Goedheer W J 1995 *J. Appl. Phys* **78** 2233
[26] Phelps A V and Petrović Z Lj 1999 *Plasma Sources Sci. Technol.* **8** R21
[27] Donkó Z 2001 *Phys. Rev.* E **64** 026401
[28] Kutasi K and Donkó Z 2000 *J. Phys. D: Appl. Phys.* **33** 1081
[29] Lawler J E 1985 *Phys. Rev. A* **32** 2977
[30] Ward A L 1962 *J. Appl. Phys.* **33** 2789
[31] Morgan W L, Boeuf J P and Pitchford L C 1998 *Siglo Data Base, CPAT and Kinema Software* http://www.csn.net/siglo
[32] Helm H and Elford M T 1978 *J. Phys* B **22** 3939
[33] Skullerud H R 1992 Private communication
[34] Massey H S W, Burhop E H S and Gilbody H B 1974 *Electronic and Ionic Impact Phenomena* vol IV (Oxford: Clarendon) p 2201
[35] Carata L, Orel A E and Suzor-Weiner A 1999 *Phys. Rev.* A **59** 2804
[36] Deloche R, Monchicourt P, Cheret M and Lambert F 1976 *Phys. Rev.* A **13** 1140
[37] Scharfetter D L and Gummel H K 1969 *IEEE Trans. Electron Devices* **16** 64
[38] Yoshida S, Phelps A V and Pitchford L C 1983 *Phys. Rev.* A **27** 2858
[39] Opal C B, Peterson W K and Beaty E C 1971 *J. Chem. Phys.* **55** 4100
[40] Birdsall C 1991 *IEEE Trans. Plasma Sci.* **19** 65
[41] Boeuf J P and Marode E 1982 *J. Phys. D: Appl. Phys.* **15** 2169
[42] Hornbeck J A and Molnar J P 1951 *Phys. Rev.* **84** 621
[43] Wellenstien H F and Robertson W W 1972 *J. Chem. Phys.* **56** 1077
[44] Collins C B, Johnson B W and Shaw M J 1972 *J. Chem. Phys.* **57** 5310
[45] Gerasimov G N and Egorova L V 1980 *Opt. Spectrosc.* **48** 566
[46] Rosen B 1970 *Spectroscopic Data Relative to Diatomic Molecules* (Oxford: Pergamon)
[47] Mulliken R S 1964 *Phys. Rev.* **136** 962
[48] Severin P J 1964 *J. Quant. Spectrosc. Transfer* **4** 763
[49] Griem H R 1963 *Phys. Rev.* **131** 1170
[50] http://cfa-www.harvard.edu/ampcgi/read_pac
[51] Francis G 1956 *Encyclopedia of Physics* vol XXII (Berlin: Springer) p 70
[52] Den Hartog E A, O'Brian T R and Lawler J E 1989 *Phys. Rev. Lett.* **62** 1500
[53] Little P F and von Engel A 1954 *Proc. R. Soc. London* A **224** 209
[54] Bouef J P and Pitchford L C 1995 *J. Phys. D: Appl. Phys.* **28** 2083
[55] Gottsho R A, Mitchell A, Scheller G R, Chan Y and Graves D B 1989 *Phys. Rev.* A **40** 6407
[56] Phelps A V 1960 *Phys. Rev.* **117** 619
[57] Hagstrum H G 1953 *Phys. Rev.* **91** 543